Experimental and numerical study on earthquake-fire coupling failure mechanism of steel cylindrical tanks

Men, Jinkun; Chen, Guohua; Reniers, Genserik; Wu, Yue; Huang, Hailing

DOI
10.1016/j.ress.2024.110016

Publication date
2024

Document Version
Final published version

Published in
Reliability Engineering and System Safety

Reliability Engineering and System Safety 245 (2024) 110016

Contents lists available at ScienceDirect

Reliability Engineering and System Safety

journal homepage: www.elsevier.com/locate/ress

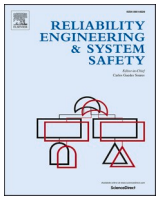

Experimental and numerical study on earthquake-fire coupling failure mechanism of steel cylindrical tanks

Jinkun Men [a,b,c], Guohua Chen [a,b,*], Genserik Reniers [c,d,e], Yue Wu [a,b], Hailing Huang [a,b]

[a] Institute of Safety Science & Engineering, South China University of Technology, No.381, Wushan Rd., Tianhe District, Guangzhou 510640, China
[b] Guangdong Provincial Science and Technology Collaborative Innovation Center for Work Safety, Guangzhou 510640, China
[c] CEDON, KU Leuven, Campus Brussels, Brussels 1000, Belgium
[d] Faculty of Technology, Policy and Management, Safety and Security Science Group (S3G), TU Delft, Delft 2628 BX, the Netherlands
[e] Faculty of Applied Economics, Antwerp Research Group on Safety and Security (ARGoSS), University Antwerp, Antwerp 2000, Belgium

ARTICLE INFO

Keywords:
Earthquake-triggered fire domino scenario
Two-stage experimental program
Steel cylindrical tanks
Coupling failure mechanism

ABSTRACT

An earthquake-triggered fire domino scenario (E-FDS) is an example of a typical multi-hazard coupling event. The seismic damage can affect the fire resistance of engineering structures, leading to significant mutually amplified phenomena. In this work, a two-stage experimental program is designed to expound the earthquake-fire coupling failure mechanism of steel cylindrical tanks (SCTs). Quasi-static tests are adopted to simulate the damage characteristics of SCTs under seismic excitation (Stage I). Fire tests are adopted to investigate the fire-resistance performance of pre-damaged SCTs (Stage II). The influences of seismic damage on the fire resistance of SCTs are particularly of interest. Three potential seismic damage degrees are considered. The experimental results show that tank specimens exhibit typical diamond-shaped buckling after Stage I. The coupling failure analysis of SCTs is conducted through sequential thermodynamic coupling simulations. Due to factors such as geometric deformation, residual stress, and thermal radiation absorption capacity, the fire resistance of SCTs is significantly attenuated by seismic damage. For the three damage states, fire resistance time attenuation coefficients (0.868, 0.716, 0.511) and critical temperature attenuation coefficients (0.910, 0.779, 0.672) were obtained. This work provides pivotal insights into the mutually amplified phenomena in E-FDSs.

1. Introduction

A chemical industrial park (CIP) can be viewed as an accident-prone safety-critical system, in which numerous hazardous installations are established to engage in high-risk industrial processes such as the storage, transportation, and production of various hazardous materials [1–3]. Large-scale earthquakes can easily trigger a series of loss of containment (LOC) events in CIPs, causing massive fires [4,5]. More alarmingly, the thermal radiation generated by fires can also cause damage to adjacent hazardous installations, and then domino effects may be triggered. As shown in Fig. 1, past accidents indicate that earthquake-triggered fire domino scenarios (E-FDSs) are one of the most prone and dangerous multi-hazard coupling events in CIPs [6–8].

The evolution of multi-hazard coupling events is complicated and dynamic, which is accompanied by significant mutually amplified phenomena [9,10]. In the past decade, some scholars have gradually realized the limitations of single-hazard studies [2,11,12]. This has driven the development of multi-hazard research. Men et al. [1,11] systematically analyzed mutually amplified phenomena between various hazards in CIPs (e.g., earthquakes, floods, hurricanes, fires, explosions), and referred to it as the term "multi-hazard coupling effect (MHCE)". According to the regional disaster system theory [13], five general forms of MHCEs are defined: *Sequential, Synchronous, Primary Scenario, Impeding Recovery,* and *Change Condition*.

The earthquake-fire sequence is one of the typical vicious cascading events associated with significant mutually amplified phenomena [1,7]. In general, E-FDSs exhibit typical characteristics of the "*Sequential*" form, that is, the first-acting seismic excitation may weaken the ability of hazard-affected objects to resist subsequent fires. As shown in Table 1, numerical simulations [14–16] and experiments [17–20] were developed to investigate the post-earthquake fire performance of various engineering structures. The knowledge extracted from simulations and experiments has provided strong evidence that seismic damage can significantly affect the fire resistance of steel structures.

Steel cylindrical tank (SCT) is one of the basic technological

* Corresponding author.
E-mail address: mmghchen@scut.edu.cn (G. Chen).

https://doi.org/10.1016/j.ress.2024.110016
Received 6 August 2023; Received in revised form 1 December 2023; Accepted 11 February 2024
Available online 13 February 2024

Abbreviations

CIP	Chemical Industrial Park
E-FDS	Earthquake-triggered Fire Domino Scenario
LOC	Loss of Containment
MHCE	Multi-hazard Coupling Effect
SCT	Steel Cylindrical Tank
RC	Reinforced Concrete

Notations

A_1	The sectional area of the tank shell, [m^2]
D_{tank}	The tank diameter, [m]
t_s	The shell thicknesses, [mm]
E	The elastic modulus, [Pa]
F_a	The constant compression load, [kN]
σ_{cr}	The allowable longitudinal compression stress, [Pa]

installations in CIPs, which has been widely used to store various inflammable, explosive and toxic hazardous materials. Past domino accidents [21–23] indicate that domino effects mainly propagate from one tank to another. However, studies concerning the failure mechanism of SCTs in E-FDSs are limited. Most of the existing studies [2,24,25] still adopt the traditional *Probit* model [26,27] to model domino effects triggered by earthquakes, ignoring the coupling effects between earthquakes and fires. Regional risks may be underestimated without full consideration of the fire resistance attenuation caused by seismic damage, potentially leading to inadequate prevention & mitigation strategies [28–30]. As a result, E-FDSs may easily result in catastrophic consequences.

Under this impetus, in this work, a two-stage experimental program and a sequential thermodynamic coupling simulation program are executed to expound the failure mechanism of SCTs exposed to the earthquake-fire sequence. The objective of this work is to provide pivotal insights into the mutually amplified phenomena associated with E-FDSs. The influences of different seismic damage degrees on the fire resistance of SCTs are particularly of interest. The fire resistance attenuation caused by minor, moderate and severe seismic damage is quantified in terms of fire resistance time and critical temperature, respectively. The importance of this work lies in its potential to significantly contribute to the fields of multi-hazard coupling fragility analysis and risk analysis.

The rest of this paper is organized as follows. In Section. 2, some preliminaries are first provided. The two-stage experimental program is stated in Section 3. The sequential thermodynamic coupling simulation program is stated in Section 4. Experimental and simulation results are analyzed and discussed in Section 5. At last, conclusions are drawn in Section 6.

2. Preliminaries

Some preliminaries about the seismic damage are stated in this section. The strong ground motion caused by large-scale earthquakes may easily impose severe structural damage on SCTs. The seismic response behavior of SCTs is extremely complex since the fluid-structure interaction system possesses many different nonlinear behavior mechanisms [3]. The seismic damage degree of SCTs is related to several factors such as earthquake characteristics, contained liquid properties and depth, dimensions of SCTs, material properties, supporting conditions and stiffness of underlying soil medium [3,31].

As shown in Figs. 2 and 3, the typical seismic damage emerges in the form of elephant foot buckling or diamond shape buckling [31]. Diamond buckling occurs at a distance above the tank base or the connection between the tank shell and the base plate. In contrast, elephant foot buckling usually appears in the lower course of the tank shell [32]. Other potential failure modes include rupture of the junction between the tank shell and base, roof damage, tank support system and foundation failure and breaking of anchor bolts [33–35]. The forms of buckling are usually caused by internal hydrodynamic (hydrostatic) pressure and vertical stresses. This phenomenon occurs when the tank shell is uplifted and rotated about its center during seismic shaking, causing vertical compression forces. The uplift can cause cracks in the tank base [31]. Sloshing waves caused by the horizontal acceleration of the convective mass can also impose severe damage to tanks. The long-period dynamic forces due to the convective wave motion can damage the roof and cause the spilling of the tank contents.

According to the experts' opinions on the seismic damage characteristics, seismic damage degrees of SCTs are usually divided into five states (DS_1: *No damage,* DS_2*: Minor damage,* DS_3*: Moderate damage,* DS_4*: Severe damage,* DS_5*: Collapsed*), the corresponding damage description is stated in Table 2. For collapsed SCTs (DS_5), subsequent fire resistance analysis is meaningless. Thus, this work only considers three seismic damage states, i.e., minor damage, moderate damage and severe damage.

3. Two-stage experimental program

Experimental specimens refer to a 5000 m^3 SCT (Steel Type: Q235, Tank Diameter: 20.000 m, Tank Height: 17.820 m, Shell Thickness: 0.013 m) designed according to the Chinese Standard GB 50,341–2014 [42]. According to the similarity principle [43,44], the similarity ratio of 50:1 is adopted to determine the geometric parameters of experimental specimens. However, as a typical thin-walled structure, it is difficult to design the tank shell thickness of specimens in the same similarity ratio. Thus, considering the experimental feasibility, the tank diameter D_{tank} = 400mm, the tank height H_{tank} = 360mm, and the shell thickness t_s = 1mm. Details of the two-stage experimental program are stated in this section, including the Stage I: Quasi-static Tests in **Section 3.1**, the Stage II: Fire Tests in **Section 3.2**

(a) (b)

Fig. 1. Post-earthquake fires related to chemical process industry. (a) Massive fires at the TUPRAS Izmit refinery in the 1999 Kocaeli earthquake [6] (b) Oil spill fires at Kesennuma Bay in the 2011 Great East Japan Earthquake and Tsunami [8].

Table 1
A summary of representative studies for investigating the coupling effects of earthquake-fire sequence.

Authors (Year)	Hazard-affected objects	Research methodologies	Main work	Extracted knowledge
Girgin (2011) [6]	Floating roof naphtha storage tanks	Accident investigation	The massive fire at the TUPRAS Izmit refinery and the acrylonitrile spill at the AKSA acrylic fiber production plant caused by the 1999 Kocaeli earthquake were investigated.	Seismic events in industrial areas may lead to additional ignition sources. Most Na-tech scenarios triggered by earthquakes show ignition probabilities that far exceed those of traditional accident scenarios. Seismic events may also damage safety barriers, lifelines and other critical infrastructures, which can greatly hinder the efficiency and effectiveness of emergency management. The seismic damage can easily aggravate the failure of storage tanks exposed to fires.
Shah et al. (2017) [17]	Reinforced concrete frames	Two-stage loading experiment	Full scale reinforced concrete (RC) frames were subjected to a predetermined earthquake damage before being exposed to a compartment fire of one-hour duration.	The increase in the severity of seismic damage leads to the formation of more wide cracks, resulting in an elevation of temperatures in the structural elements of RC frames.
Talebi et al. (2018) [14]	Concrete filled steel tube columns	Finite element simulation and analysis	A nonlinear three-dimensional finite element model was developed to investigate the response of concrete filled tube columns exposed to post-earthquake fires.	Simulation results indicate that the column with the middle span damage performed a lesser fire resistance time owing to the coincidence of the damage location to that of the onset of global buckling.
Vitorino et al. (2020) [15]	Reinforced concrete elements	Finite element simulation and analysis	Numerical simulations were performed to investigate effects of earthquake damage on the fire resistance of RC elements.	Simulation results show that seismic damage can significantly reduce the fire resistance of RC elements, especially if the cover of the elements is removed and the reinforcement is exposed to fire.
Wang et al. (2021) [18]	Square concrete-filled steel tube columns	Quasi-static and fire test experiment	An experimental program that contains quasi-static tests and fire tests was developed to investigate the post-earthquake fire performance of concrete-filled steel tube columns.	The fire resistance of specimens is significantly affected by the degree of seismic damage. The more serious seismic damage results in less fire resistance time of concrete-filled steel tube columns.
Alasiri et al. (2021) [16]	Steel moment frame buildings	Finite element simulation and analysis	A numerical simulation method was developed to assess post-earthquake fire performance of steel moment frame buildings.	Gravity columns are the most critical system component, since interior compartment fires can result in overall system collapse after gravity column failure initiation.
Calayir et al. (2022) [19]	Fire doors	Cyclic and fire test experiment	An experimental cyclic and fire test program was developed to investigate post-earthquake fire performance of fire door set.	Experimental results indicate that the fire resistance of the fire door sets with seismic damage decreases by as much as 70 %. The reduction can be attributed to large gaps due to the distorted door geometry after seismic loading, substantial loosening of the door hinges and damaged intumescent seals around the door.
Lou and Wang (2022) [20]	Specimens of Q235 steel	Two-stage loading experiment	The procedure of a two-stage damage experiment was designed to investigate the material properties of mild steel with different seismic damage states at elevated temperatures. The pre-strain amplitude and the temperature were considered	The elastic modulus of Q235 specimens is obviously affected by the degree of seismic damage. Compared to the non-pre-damaged group, at least a 15 % reduction of modulus can be observed in the group with extremely severe pre-damage at each level of

(*continued on next page*)

Table 1 (*continued*)

Authors (Year)	Hazard-affected objects	Research methodologies	Main work	Extracted knowledge
			to be the crucial variables.	elevated temperature. Thermal effects dominate the development of ultimate strength, while the amplitude of pre-strain appears to have a negligible impact on it.

3.1. Stage I: quasi-static tests

In stage I, the quasi-static tests are adopted to simulate the damage characteristics of SCTs under seismic excitation. Experimental specimens are loaded under constant compressive force and cyclic horizontal force. The quasi-static tests can effectively simulate the stress characteristics and deformation characteristics of SCTs in the reciprocating vibration during the earthquake [3,14,16]. The specific test device system and the loading criterion are stated in the following sub-sections.

3.1.1. Test device system

The quasi-static test device system is shown in Fig. 4, which is mainly composed of the tank specimen, the tank roof, the anchor base, the electro-hydraulic servo loading system ZB-ZD3000, the hydraulic cylinder HC-30, the strain test system JM3841, the PC 610 L, the reaction wall, the strain gauges BFH120–5AA-D150, the MOOG servo valve G631, and the motion detector YHD-500 L.

During the quasi-static tests, the electro-hydraulic servo loading system ZB-ZD3000 and the hydraulic cylinder HC-30 are connected to an experimental specimen using a top attachment, which is a steel tank roof. The top attachment has a circular groove with a depth of 20 mm, and the tank shell has reserved 20 mm for the reinforcement of the top attachment. The reserved part can be regarded as a rigid body. The bottom of the specimen is required to be anchored to the ground. The base attachment is used to anchor the tank bottom to the ground. In addition, a rotatable threaded rod is connected to the hydraulic cylinder HC-30. This is used to ensure that the horizontal load is always centered on the center of the tank roof while the vertical load is applied.

3.1.2. Loading criterion

Following the standard loading criterion [3,18], the constant compression load F_a is considered to be 30 % of the allowable longitudinal compression stress σ_{cr}. According to the Chinese Standard GB 50, 341–2014 Annex D [42], the allowable longitudinal compression stress

Table 2
Five seismic damage states [39–41].

Notations	Damage State	Physical Damage Description
DS_1	No damage	No damage to tank structure and accessories
DS_2	Minor	Damage to roof, minor loss of content, minor shell damage, minor piping damage, cracked foundation of the tank, no buckling
DS_3	Moderate	Buckling with no leak or minor loss of contents
DS_4	Severe	Buckling with major loss of contents, severe damage
DS_5	Collapsed	Total failure, tank structure collapse

(a) (b)

Fig. 2. Diamond-shaped buckling of steel tanks, (a) Diamond-shaped buckling of a steel tank during the Silakhor Earthquake of 2006 in Iran [36]; (b) Diamond-shape buckle of a steel tank in Kobe at the 1995 Kobe Earthquake [37].

(a) (b)

Fig. 3. Elephant-foot buckling and cracked foundation of steel tanks, (a) Elephant-foot buckling of a tank wall (courtesy of University of California at Berkeley) [38]; (b) Cracked foundation of the tank during the Silakhor Earthquake of 2006 in Iran [34].

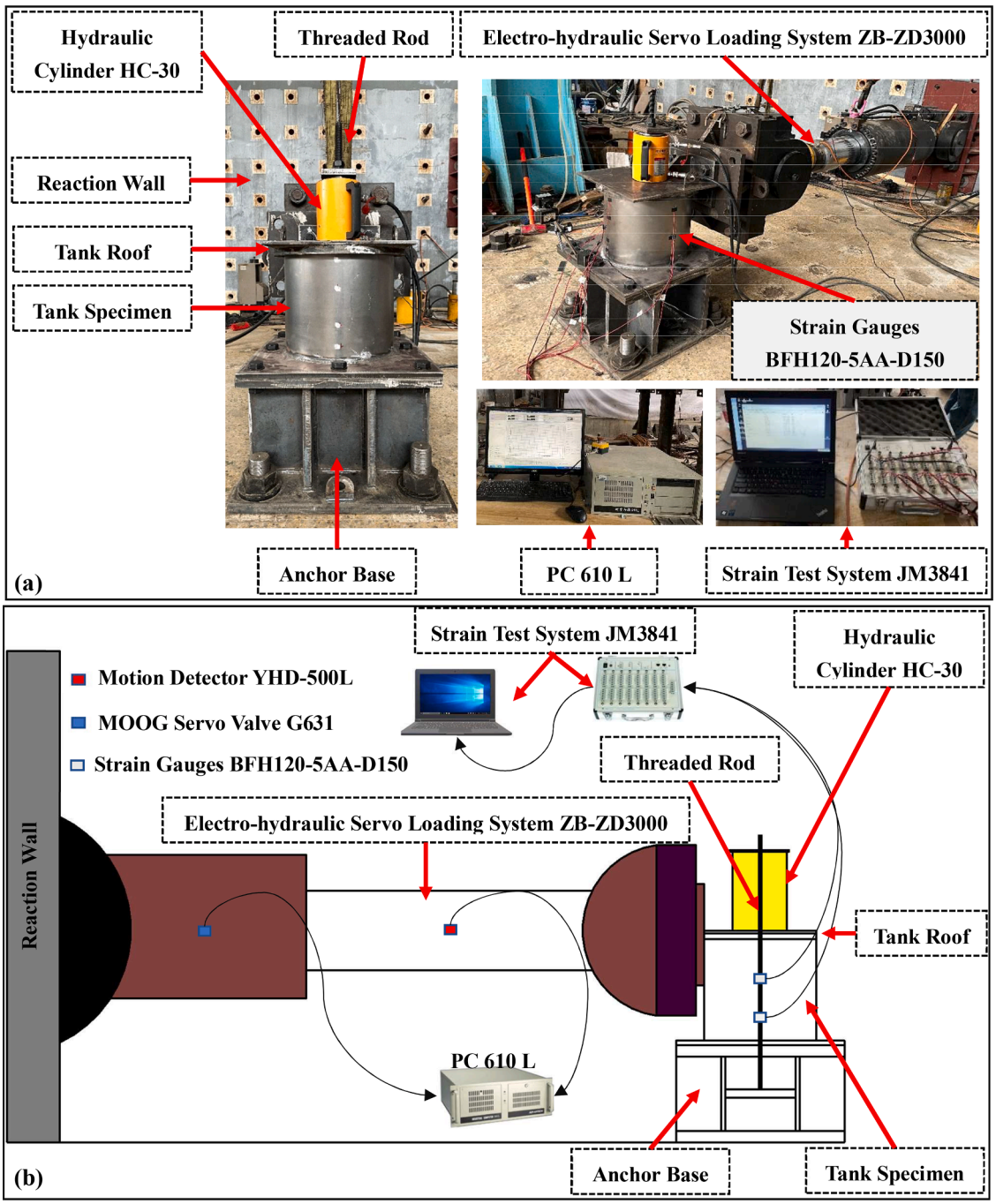

Fig. 4. The quasi-static test device system, (a) physical diagram; (b) schematic diagram.

σ_{cr} can be calculated as follows:

$$\sigma_{cr} = 0.22E\frac{t_s}{1000D_{tank}} \approx 1.133e + 08\text{Pa} \tag{1}$$

where $E = 2.06e + 11$Pa is the elastic modulus of Q235 steel; $t_s = 1$mm is the shell thicknesses; $D_{tank} = 0.4$m is the tank diameter. The constant compression load applied to the top of tank F_a was chosen as 30 % of the ultimate bearing capacity of specimens [18].

$$F_a = 0.3\sigma_{cr}A_1 \approx 44.187\text{kN} \tag{2}$$

where $A_1 = \pi(R^2 - (R - t_s)^2) = 0.0013$ m^2.

With the consideration of the weight of the tank roof, a constant axial force of 42.6kN is applied during the quasi-static tests. As illustrated in Fig. 5, the horizontal cyclic load is applied to experimental specimens using displacement control. The initial displacement is set to 1 mm, with two cycles of load applied at each level, followed by a progressive increment of 0.5 mm in subsequent levels.

3.2. Stage II: fire tests

Escalation vectors responsible for the escalation of fire domino accidents in chemical industries are stated in Table. 3 [45]. Accordingly, as shown in Fig. 6, the fire tests considered three fire domino scenarios. For **Scenario 1**, a circular oil tray with a diameter of 0.3 m at a distance of 0.1 m from the damaged side of specimens (the positive y-direction) is ignited. The elevation of the tank shell temperature is attributed to the thermal radiation emitted by the pool fire.

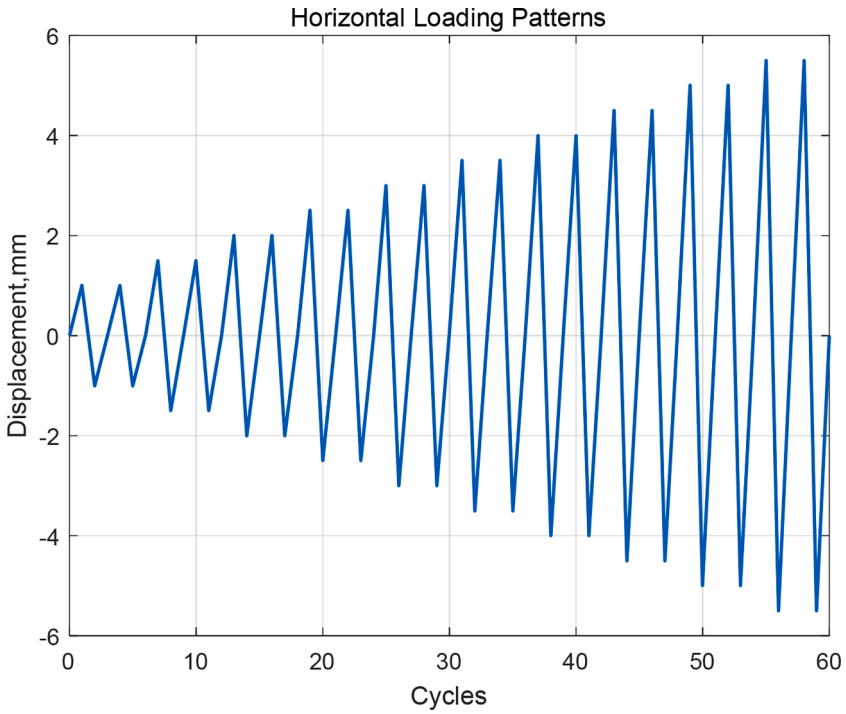

Fig. 5. Horizontal loading patterns.

Table 3
Escalation vector responsible for the escalation of fire domino accidents [45].

Primary scenario	Escalation vector	Expected Secondary Scenarios
Pool fire	Radiation, fire impingement	Jet fire, pool fire, BLEVE, toxic release
Jet fire	Radiation, fire impingement	Jet fire, pool fire, BLEVE, toxic release
Fireball	Radiation, fire impingement	Tank fire
Flash fire	Fire impingement	Tank fire

For **Scenario 2**, the circular oil tray is positioned at the central location within the interior of specimens. For **Scenario 3**, the tank specimen is immersed in a quadrate oil tray with a length of 0.6 m, simulating the typical enclosure of storage tanks within square bund walls in actual chemical tank areas. For **Scenarios 2** and **3,** the elevation of the tank shell temperature is attributed to the fire impingement emitted by the pool fire.

As illustrated in Fig. 7, three K-type thermocouples are installed in each coordinate axis direction, and the Fluke Thermal Imager Ti400 is employed to capture the temperature distribution on the tank shell. The Data Acquisition System 34970A is utilized for capturing the thermocouple data. Jet-A aviation kerosene is used as the fuel.

4. Finite element analysis

The finite element analysis (FEA) model is established using Abaqus software. The flowchart of the proposed FEA is illustrated in Fig. 8. The material property parameters of Q235 steel used in the model are presented in Tables 4 and 5.

Stage I quasi-static tests are modeled using the *Static, General* module in Abaqus software. Stage II fire tests were modeled using the *Heat*

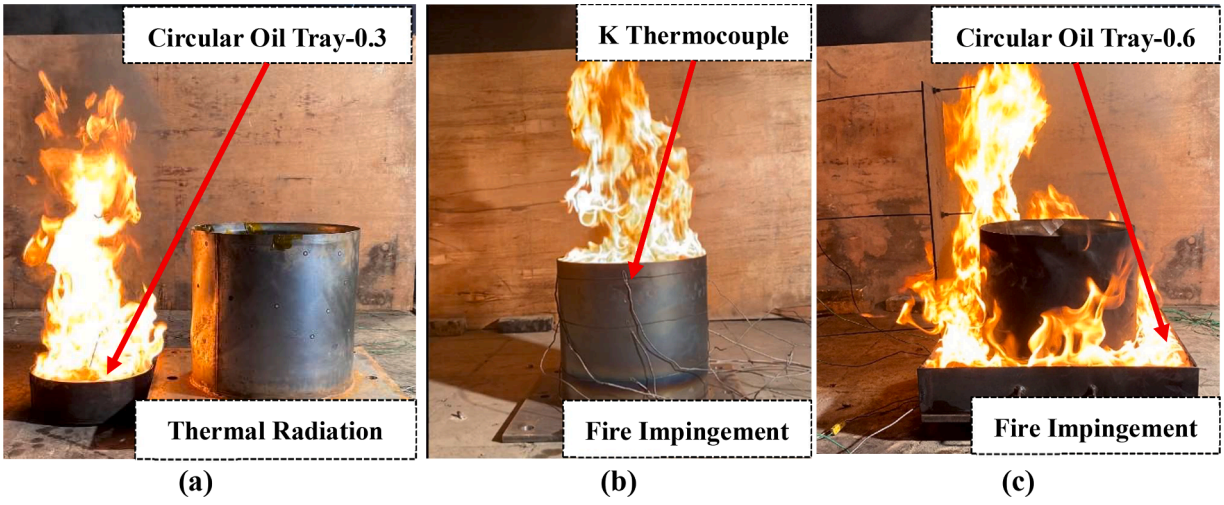

Fig. 6. Three fire domino scenarios, (a) Fire Scenario 1; (b) Fire Scenario 2; (c) Fire Scenario 3.

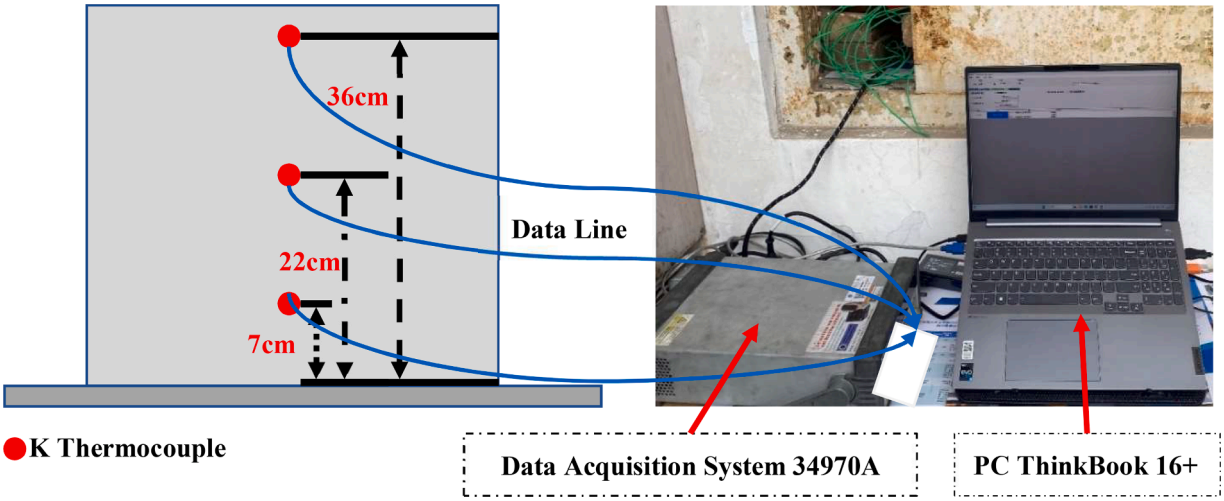

Fig. 7. The schematic diagram of the fire test.

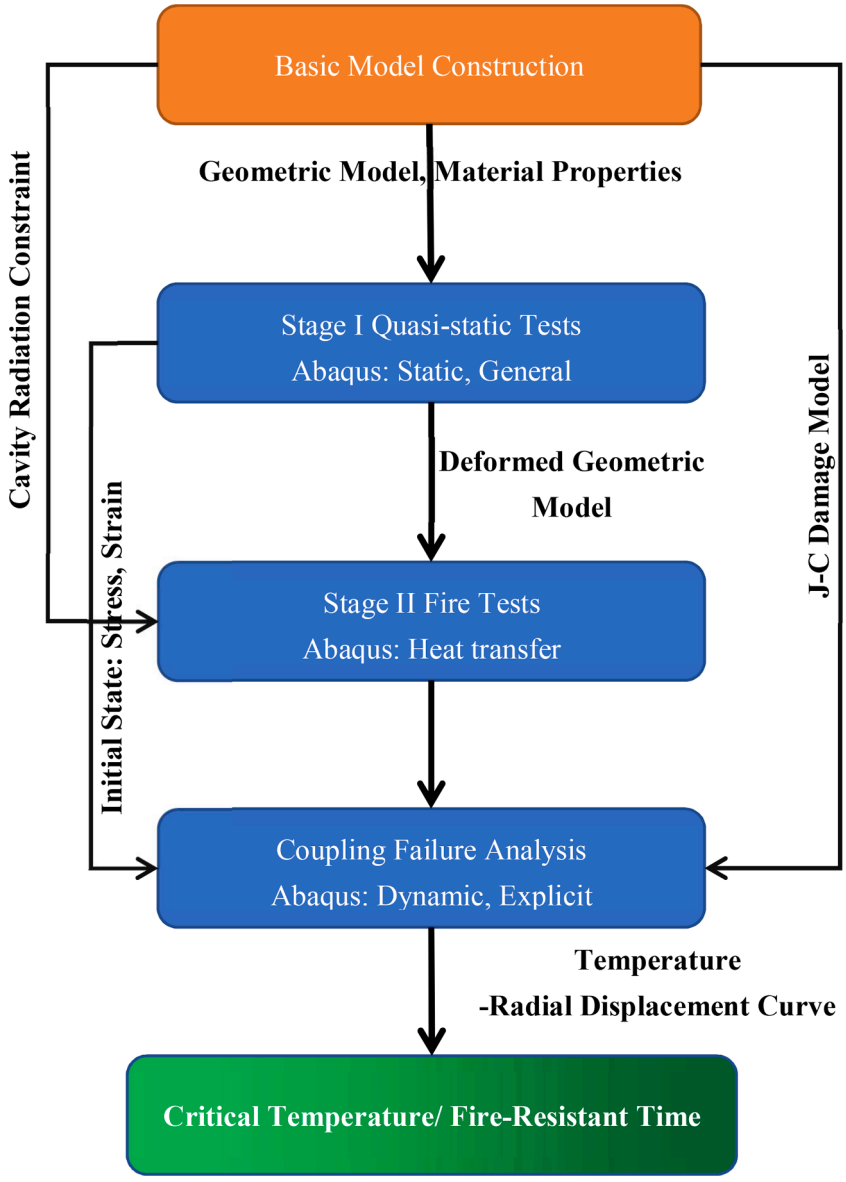

Fig. 8. The flowchart of finite element analysis.

Table 4
Material properties of Q235 steel at different temperatures [43,48,49].

Temperature (°C)	Density (kg/m^3)	Young Modulus (MPa)	Poisson ratio	Thermal conductivity (W/(m·°C))	Specific heat (J/(kg·°C))	Thermal Expansion Coefficient (/°C)
20	7850	2.06e+5	0.30	44	460	1.20e-5
100	7850	2.01e+5	0.29	44	460	1.26e-5
200	7850	1.95e+5	0.28	44	460	1.34e-5
300	7850	1.83e+5	0.27	44	460	1.42e-6
400	7850	1.69e+5	0.26	44	460	1.50e-5
500	7850	1.26e+5	0.25	44	460	1.58e-5
600	7850	0.35e+5	0.24	44	460	1.66e-5

Table 5
Johnson-Cook parameters of Q235 steel [50,51].

A (MPa)	B (MPa)	n	C	m	Reference temperature (°C)	Melting temperature (°C)
293.8	230.2	0.578	0.0652	0.706	20	1500
D_1	D_2	D_3	D_4	D_5	D_6	Reference strain rate (s^{-1})
0.472	18.728	−7.805	−0.0193	13.017	2.338	0.021

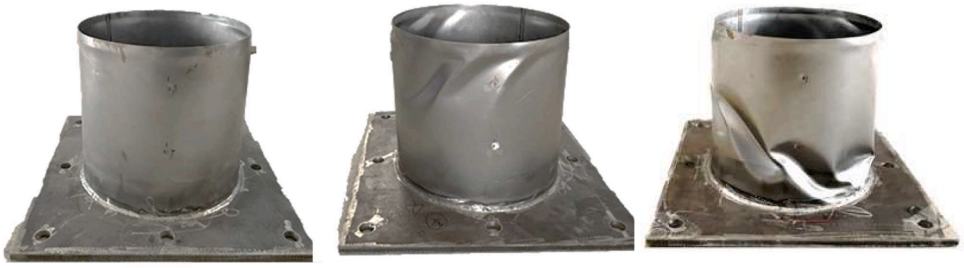

Fig. 9. The pre-damaged tanks after quasi-static tests, (a) DS_2; (b) DS_3; (c) DS_4.

Transfer module in Abaqus. The deformed geometric models obtained by quasi-static tests are adopted for cavity thermal radiation analysis. The solid flame model is developed with 0.8 cavity heat radiation [46,47]. The coupling failure analysis of SCTs is developed through the sequential thermodynamic coupling simulation using the *Dynamic, Explicit* in Abaqus software. By utilizing restart techniques, particular attention is given to the residual stresses and geometric deformations of the pre-damaged tanks.

5. Results and discussion

5.1. Experimental results of stage I

5.1.1. Geometric deformation characteristics

The pre-damaged tanks after quasi-static tests are shown in Fig. 9. The experimental results show that tank specimens exhibit typical diamond-shaped buckling after Stage I. To achieve different seismic damage states, specimens were loaded to different load levels. For damage state DS_2, specimens were loaded up to the fourth level of loading (2.5 mm) and then unloaded. As shown in Fig. 9(a), there is a slight buckling observed in the tank shell. For damage state DS_3, specimens were loaded up to the eighth level of loading (4.5 mm) and then unloaded. As shown in Fig. 9(b), there is a significant diamond-shaped buckling observed in the tank shell. For damage state DS_4, specimens were loaded up to the tenth level of loading (5.5 mm), which can be regarded as the ultimate horizontal load. As shown in Fig. 9(c), the tank shell experiences severe diamond-shaped buckling and collapse. Additionally, the vertical load has become difficult to stably apply to the tank roof. The comparison between Fig. 3(a,b) and Fig. 9 indicates that the geometric deformation characteristics of pre-damaged specimens closely match those of the damaged SCTs in real seismic scenarios.

5.1.2. Displacement-force hysteresis curves

The displacement-force hysteresis curves obtained by quasi-static tests refer to the red lines in Fig. 10. The experimental results indicate that the horizontal reaction force of specimens increases with the increase in displacement load. As shown in Fig. 10(a), when the peak of the horizontal displacement load reaches 2.5 mm, the maximum reaction force measured is 27.990 kN, which has not reached the horizontal bearing capacity limit of the specimen yet. As shown in Fig. 10(a), when the peak of the horizontal displacement load reaches 4.5 mm, the maximum reaction force measured is 48.710 kN, nearly reaching the horizontal load-carrying capacity limit of the specimen. As shown in Fig. 13(c), when the peak of the horizontal displacement load reaches 5.5 mm, the maximum reaction force measured is 48.830 kN. The horizontal bearing capacity limit of this severely damaged specimen dropped to 25.630 kN (52.488 % of the peak capacity).

The displacement-force hysteresis curves obtained by FEA refer to the blue lines in Fig. 10. Compared to the results of FEA, the experimental curve exhibits a “pinching” phenomenon with a longer sliding segment. This is attributed to the presence of small gaps between the tank roof and the tank shell.

5.2. Finite element analysis results of stage I

5.2.1. Comparative analysis of geometric deformation

The corresponding FEA results of Stage I are shown in Figs.11-13. By comparing Fig. 9 and Fig. 10, it can be observed that the geometry deformation of tanks obtained from the FEA closely matches the experimental results. Both exhibit the typical diamond-shaped buckling seismic damage characteristics. The diamond-shaped buckling of the tank shell is primarily caused by the combined effects of compressive forces and shear forces [3,34,40].

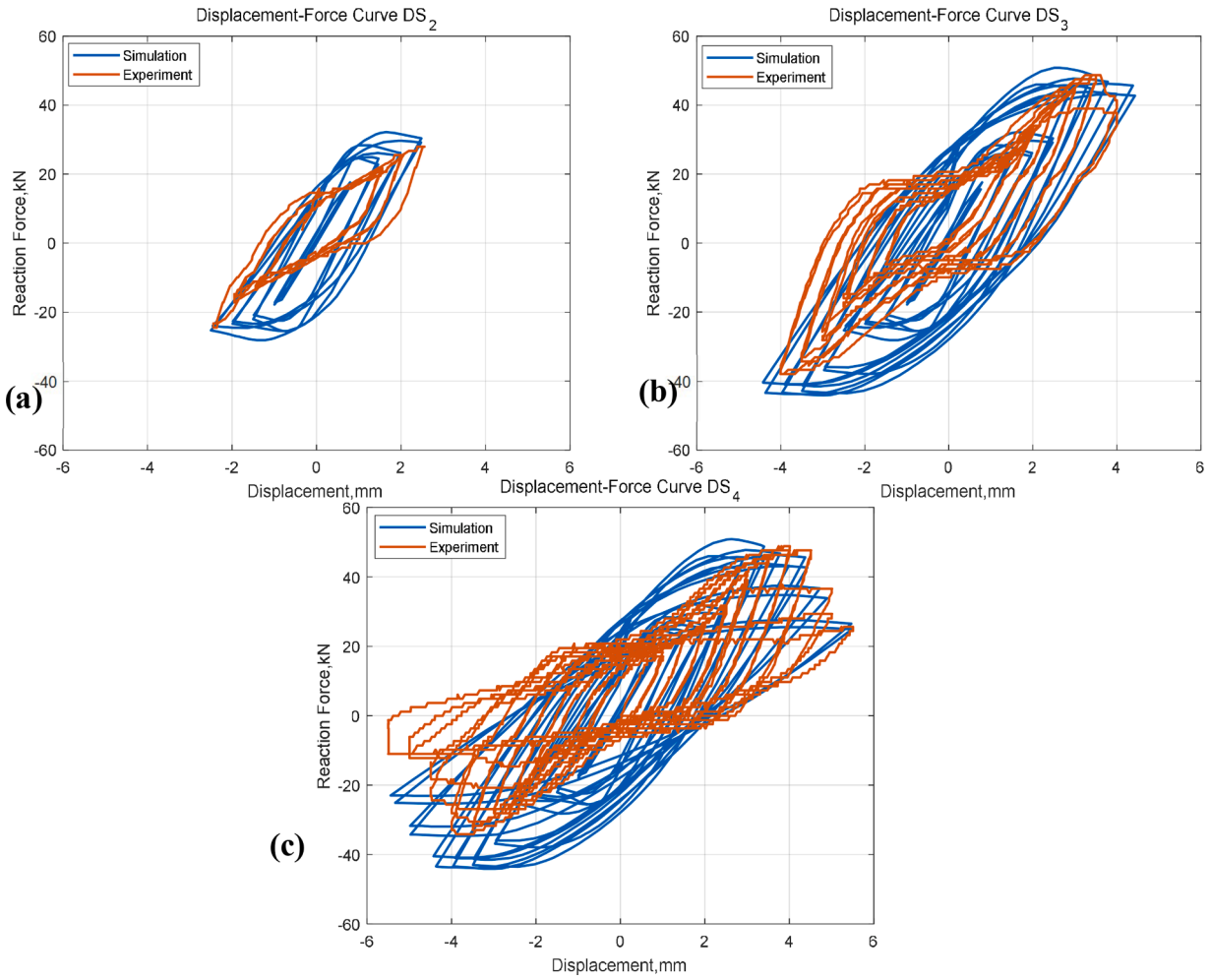

Fig. 10. The displacement-force hysteresis curve, (a) DS_2; (b) DS_3; (c) DS_4.

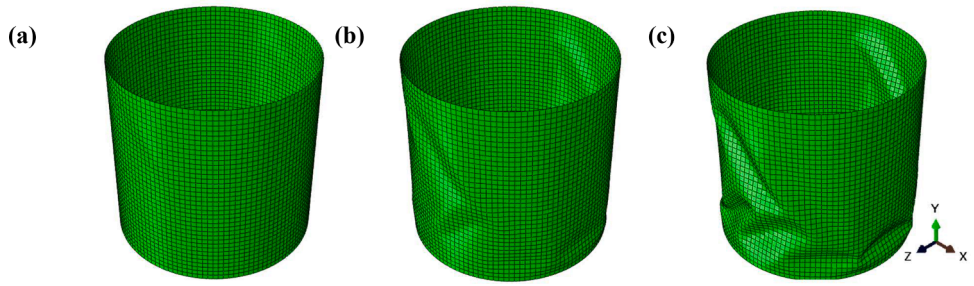

Fig. 11. Finite element analysis results of Stage I-Geometry Deformation, (a) DS_2; (b) DS_3; (c) DS_4.

As shown in Fig. 12, FEA results indicate that for a minorly damaged tank (DS_2), the maximum deformation displacement is 1.818 mm; for a moderately damaged tank (DS_3), the maximum deformation displacement is 6.488 mm; for a severely damaged tank (DS_4), the maximum deformation displacement is 25.580 mm.

As shown in Fig. 13, FEA results indicate that for a minorly damaged tank (DS_2), the maximum residual stress is 2.563e+08 Pa; for a moderately damaged tank (DS_3), the maximum residual stress is 3.810e+08 Pa; for a severely damaged tank (DS_4), the maximum residual stress is 4.716e+08 Pa.

5.2.2. Comparative analysis of damage characteristics

To obtain the seismic-damaged specimens required for the Stage II fire test, two sets of repeated experiments were conducted for each damage state. A comparative analysis of the experimental results and FEA results can be found in Tables 6-8 (experimental results are highlighted in bold). The maximum reaction force, the maximum deformation displacement, the final horizontal bearing capacity, and the maximum residual strain are compared to validate the reliability of the FEA model. During the quasi-static tests, the values of maximum residual strain are measured by strain gauges. The maximum residual stress measured by strain gauges and the corresponding FEA results at the same location are compared. Moreover, the values of maximum residual strain obtained by FEA are also listed in Tables 6-8 (see the results within the brackets).

Measurement errors, specimen standards, boundary conditions, or

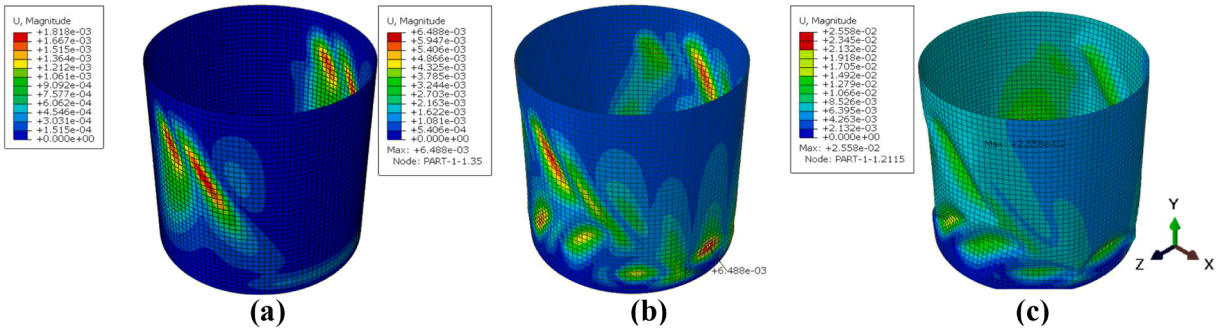

Fig. 12. Finite element analysis results of Stage I-Displacement, (a) DS_2; (b) DS_3; (c) DS_4.

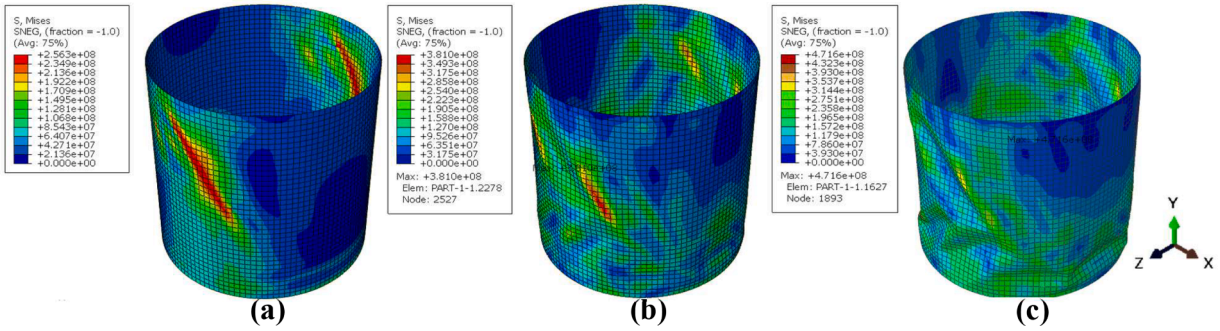

Fig. 13. Finite element analysis results of Stage I- Mises Stress, (a) DS_2; (b) DS_3; (c) DS_4.

Table 6
Comparative analysis results of Stage-I (DS_2).

	Maximum Reaction Force (kN)	Maximum Deformation Displacement (mm)	Maximum Residual Strain
Specimen 1-DS_2	**27.990**	**1.725**	**3.143e-03**
Specimen 2-DS_2	**28.132**	**1.571**	**3.456e-03**
Specimen 3-DS_2	**28.997**	**1.536**	**3.611e-03**
Average	**28.373**	**1.611**	**3.403e-03**
FEA	32.164	1.818	3.621e-03 (4.130e-03)
Error	+13.361 %	+12.870 %	+6.397 %

Table 7
Comparative analysis results of Stage-I (DS_3).

	Maximum Reaction Force (kN)	Maximum Deformation Displacement (mm)	Final Horizontal Bearing Capacity (kN)	Maximum Residual Strain
Specimen 4-DS_3	**48.710**	**7.015**	**38.919**	**1.012e-02**
Specimen 5-DS_3	**46.316**	**7.082**	**39.799**	**1.089e-02**
Specimen 6-DS_3	**51.072**	**6.954**	**40.611**	**9.931e-03**
Average	**48.699**	**7.017**	**39.793**	**1.031e-02**
FEA	50.853	6.488	42.714	9.213e-03 (1.191e-02)
Error	+4.422 %	−7.538 %	+7.340 %	−10.676 %

material models could all potentially contribute to discrepancies between experimental results and FEA results. The comparative analysis indicates that the error in various parameters spans from 2.0 % to 13.4 %, falling within an acceptable range [17,20,43]. Furthermore, we found that for specimens 1, 2 and 3, the errors are relatively larger. This is mainly caused by the gaps between the tank shell and the tank roof. Due to the gaps, the horizontal displacement load applied by the electro-hydraulic servo loading system is somewhat reduced. Thus, values of maximum reaction force obtained by FEA are slightly larger than experimental results. To obtain minorly damaged specimens, the horizontal displacement load is relatively small. In this situation, the load reduction is more significant, leading to relatively larger errors.

Table 8
Comparative analysis results of Stage-I (DS_4).

	Maximum Reaction Force (kN)	Maximum Deformation Displacement (mm)	Final Horizontal Bearing Capacity (kN)	Maximum Residual Strain
Specimen 7-DS_4	**48.830**	**24.325**	**25.630**	**4.034e-02**
Specimen 8-DS_4	**50.121**	**23.382**	**26.998**	**3.921e-02**
Specimen 9-DS_4	**49.725**	**26.778**	**23.562**	**3.887e-02**
Average	**49.558**	**24.828**	**25.398**	**3.950e-02**
FEA	50.853	25.580	24.886	3.782e-02 (4.959e-02)
Error	+2.613 %	+3.029 %	−2.016 %	−4.253 %

The experimental results still closely align with the FEA results, demonstrating a good agreement between quasi-static tests and FEA. For specimens 4∼9, their horizontal bearing capacity limits are 48.710 kN, 46.316 kN, 51.072 kN, 48.830 kN, 50.121 kN, 49.725 kN respectively. Correspondingly, the average horizontal bearing capacity limit for the specimens is 49.629 kN, which closely matches the FEA result (50.853 kN). Moreover, as shown in Table 8, experimental results indicate that the average horizontal load-carrying capacity limit dropped to 51.2 % of the peak capacity while specimens are severely damaged.

Fig. 14. The structure of the pool fire plume.

5.3. Experimental results of stage II

5.3.1. Flame combustion characteristics

The fire tests were conducted with negligible wind conditions. The Jet-A-1 aviation kerosene was selected as the fuel for the pool fire. The density of Jet-A-1 is 802 kg/m^2. The flow of the flame above the fuel and the combustion-generated smoke is commonly referred to as the plume [52].

As shown in Fig. 14, the plume of a pool fire is mostly characterized by a naturally spreading flame, and its flow is governed by buoyancy. As the liquid fuel continues to evaporate and burn, the plume continuously entrains fresh, cool air from the surroundings and transports mass and heat upward. The pool fire plume can typically be divided into three zones, i.e., the continuous flame zone, intermittent flame zone and smoke plume zone.

The flame combustion characteristics of three fire scenarios are shown in Fig. 15. Experimental results indicate that the temperature in the fuel surface region is relatively low. In the continuous flame zone, the flame temperature increases with height. In the intermittent flame zone, the temperature variation along the axial height is more chaotic, and there is a significant level of dispersion. To be specific, for fire scenario 1, the maximum flame height is 0.740 m, and the maximum flame temperature can reach up to 8.103e+02 ℃; for fire scenario 2, the maximum flame height is 0.820 m, and the maximum flame temperature can reach up to 8.450e+02 ℃; for fire scenario 3, the maximum flame height is 0.780 m, and the maximum flame temperature can reach up to 8.787e+02 ℃.

5.3.2. Thermal response analysis

For fire scenario 1, the pool fire was placed 0.1 m directly in front of the damaged side of specimens (the positive y-direction). The tank shell temperature gradually increases due to the thermal radiation from the pool fire.

As shown in Fig. 16(a), the high-temperature region is mainly distributed in the middle section of the tank shell on the fire-exposed side. In fire scenario 1, the maximum tank shell temperatures of DS_1, DS_2, DS_3, DS_4 tank specimens are 180.276 °C, 175.681 °C, 177.276 °C, 173.276 °C, respectively. The corresponding fire exposure time to reach the highest temperature is 283 s, 281 s, 277 s, and 278 s, respectively. Thermal radiation heating occurs when a SCT absorbs external radiation energy, conducts heat internally, and exchanges heat with the environment, resulting in a gradual increase in the tank shell temperature [46,47,52]. Geometric deformation of a pre-damaged specimen alters the surface characteristics of its tank shell, thereby affecting the radiation absorption capacity of the shell surface. Consequently, the maximum shell temperature of pre-damaged specimens is slightly lower than that of intact specimens.

For fire scenario 2, the tank shell temperature gradually increases due to the flame impingement from the pool fire. As shown in Fig. 16(b),

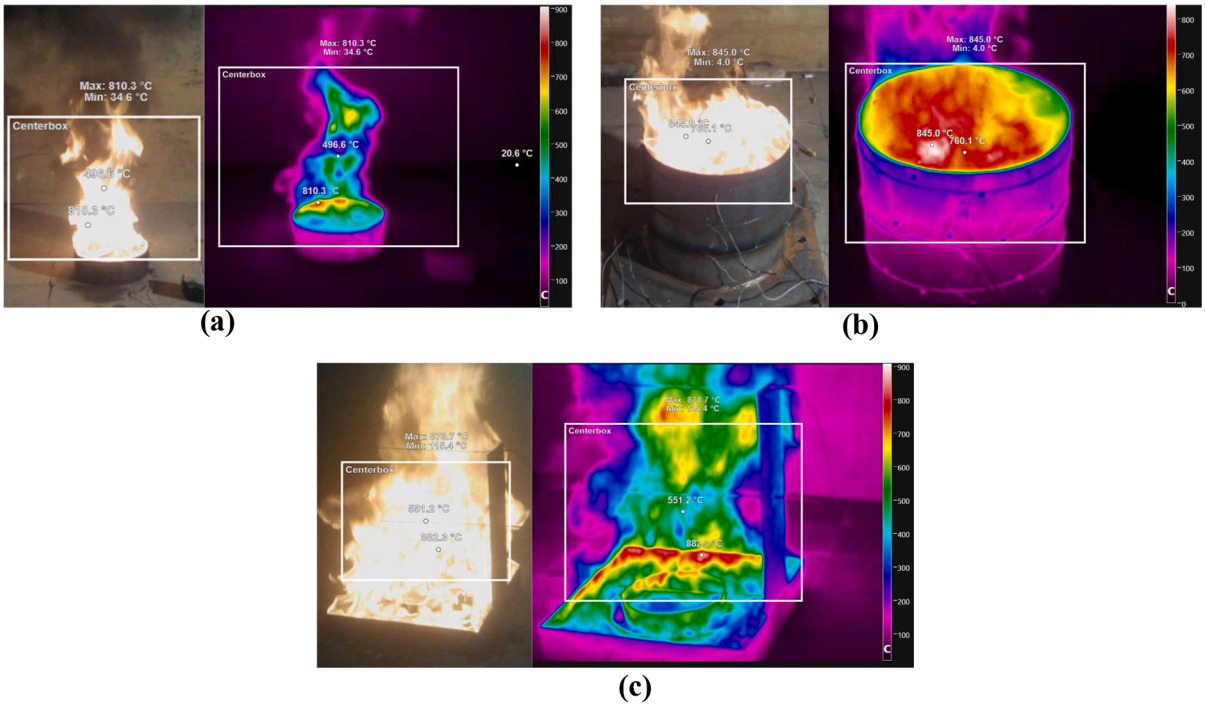

Fig. 15. Flame combustion characteristics, (a) Fire Scenario 1; (b) Fire Scenario 2; (c) Fire Scenario 3.

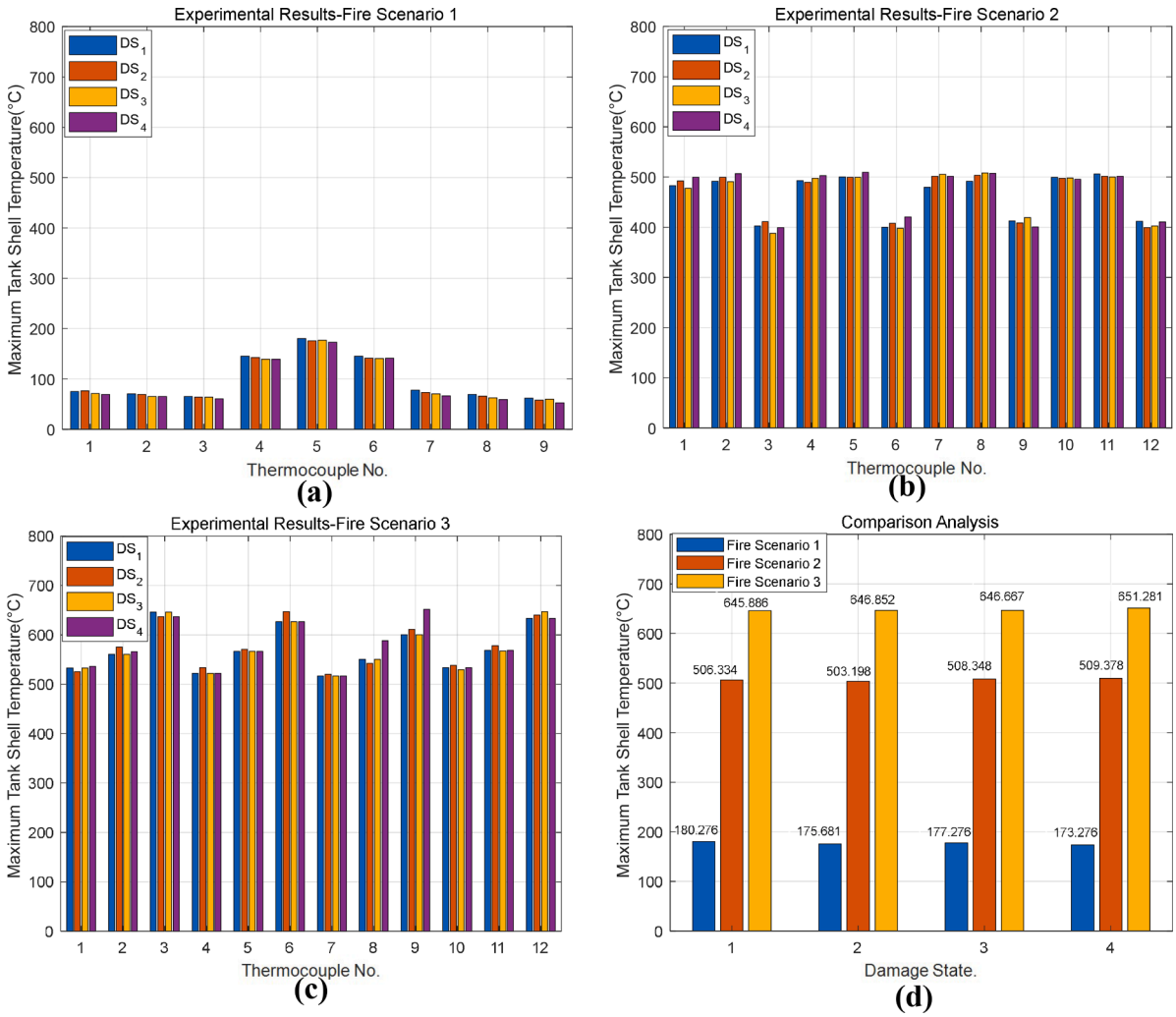

Fig. 16. Maximum tank shell temperature, (a) Fire Scenario 1; (b) Fire Scenario 2; (c) Fire Scenario 3; (d) Comparison Analysis.

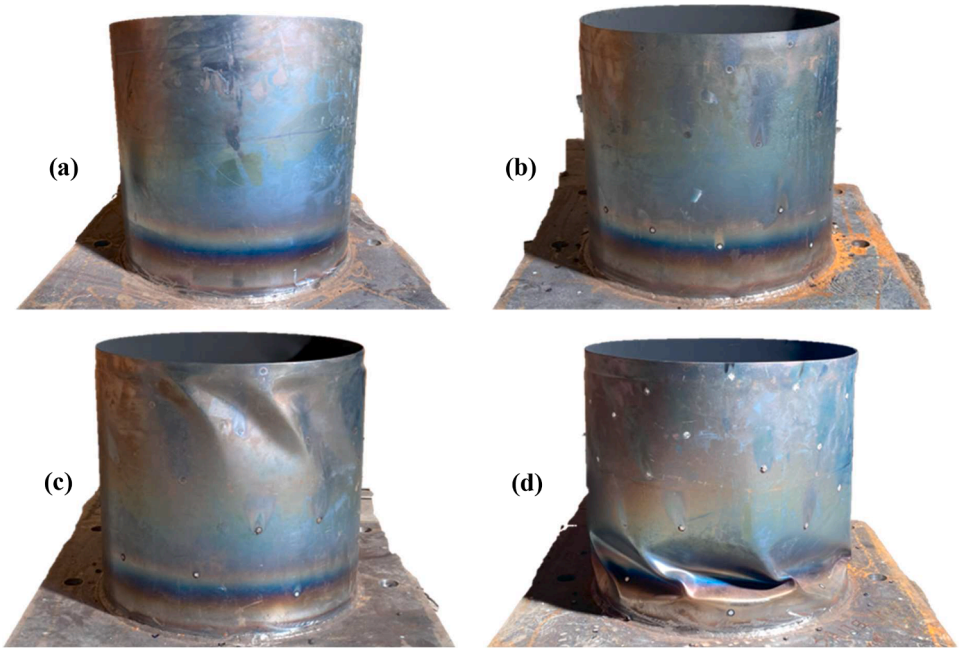

Fig. 17. "Blue Brittle" of the tank shell in Fire Scenario 2, (a) DS_1; (b) DS_2; (c) DS_3; (d) DS_4.

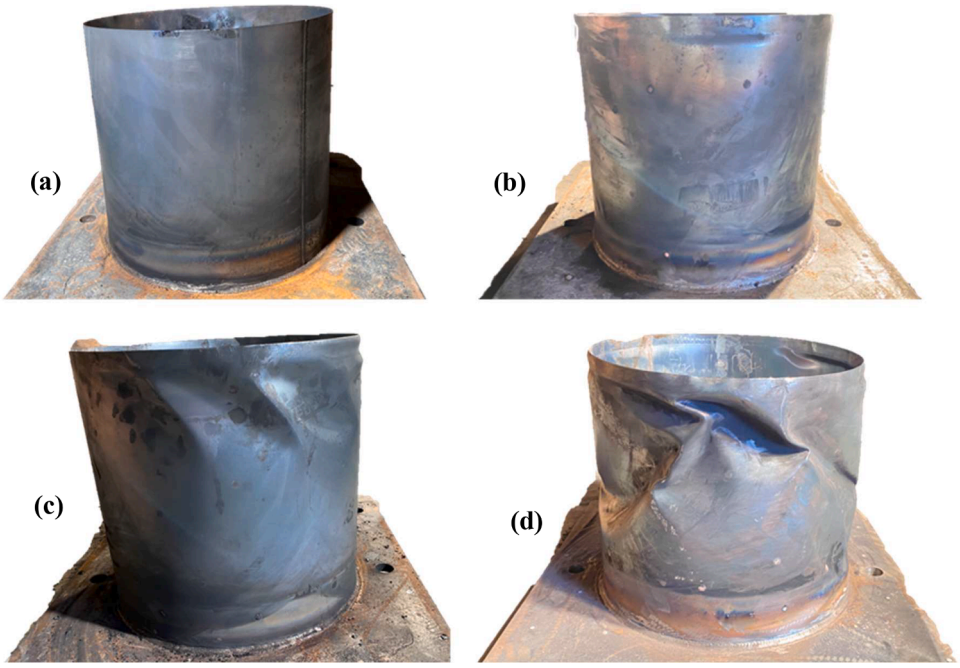

Fig. 18. "Blue Brittle" of the tank shell in fire scenario 3, (a) DS_1; (b) DS_2; (c) DS_3; (d) DS_4.

the high-temperature region is primarily distributed in the middle and upper sections of the tank shell. In fire scenario 2, the maximum tank shell temperatures of DS_1, DS_2, DS_3, DS_4 tank specimens are 506.334 °C, 503.198 °C, 508.348 °C, 509.378 °C, respectively. The corresponding fire exposure time to reach the highest temperature is 134 s, 128 s, 122 s, and 123 s, respectively.

For fire scenario 3 shown in Fig. 16(c), the high-temperature region is primarily distributed in the lower section of the tank shell. In fire scenario 3, the maximum tank shell temperatures of DS_1, DS_2, DS_3, DS_4 specimens are 645.886 °C, 646.852 °C, 646.666 °C, 651.281 °C, respectively. The corresponding fire exposure time to reach the highest temperature is 174 s, 176 s, 170 s, and 166 s, respectively.

As shown in Figs. 17 and 18, tank shells in fire scenarios 2 and 3 show a distinct "blue brittle" phenomenon, which is mainly associated with grain growth and intergranular corrosion in the Q235 steel. At high temperatures, the grains in the steel tend to grow larger, and the characteristics of the grain boundaries change. Intergranular corrosion at high temperatures weakens the grain boundary regions, leading to reduced toughness and tensile strength of the tank shell. It may also promote hydrogen accumulation, further increasing the risk of brittle fracture.

For fire scenarios 2 and 3, it can be observed that the maximum tank shell temperatures of pre-damaged specimens are higher than that of intact specimens. The geometric deformation may result in localized thinning of the tank shell, which can reduce the heat capacity of deformation areas, causing the temperature to rise more rapidly compared to the undamaged sections of the tank shell. Additionally, the geometric deformation may also affect the distribution of heat and flame impingement on the tank shell. Distorted or displaced sections of the tank shell may be more exposed to direct flame contact, leading to localized hotspots and increased temperature gradients. The combination of the thinning of the tank shell and the altered heat distribution can result in higher and more rapid temperature increases in the damaged regions compared to the undamaged sections of specimens.

5.4. Finite element analysis results of stage II

5.4.1. Comparative analysis of tank shell temperature

Following the related studies [46,47,52], the static flame model is adopted to model the thermal response of fire scenario 1. The schematic diagram of the static flame model is shown in Fig. 19. According to the experimental results, the flame height is set to 0.7 m. According to the calculation method provided in the literature [53], the equivalent temperature of the solid flame is set to 485 °C.

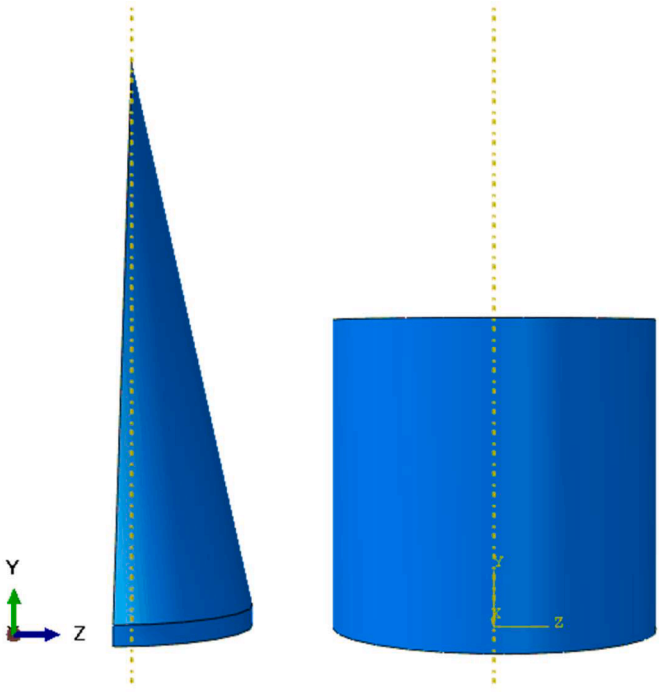

Fig. 19. The schematic diagram of the static flame model.

FEA results of Stage II are shown in Fig. 20. It can be observed that the temperature distribution on the tank shell is consistent with the experimental results. The high-temperature region is primarily concentrated in the middle section of the tank shell. Simulation results indicate that the maximum tank shell temperatures of DS_1, DS_2, DS_3, DS_4 tank specimens are 194.288 °C, 194.502 °C, 192.813 °C, 189.395 °C,

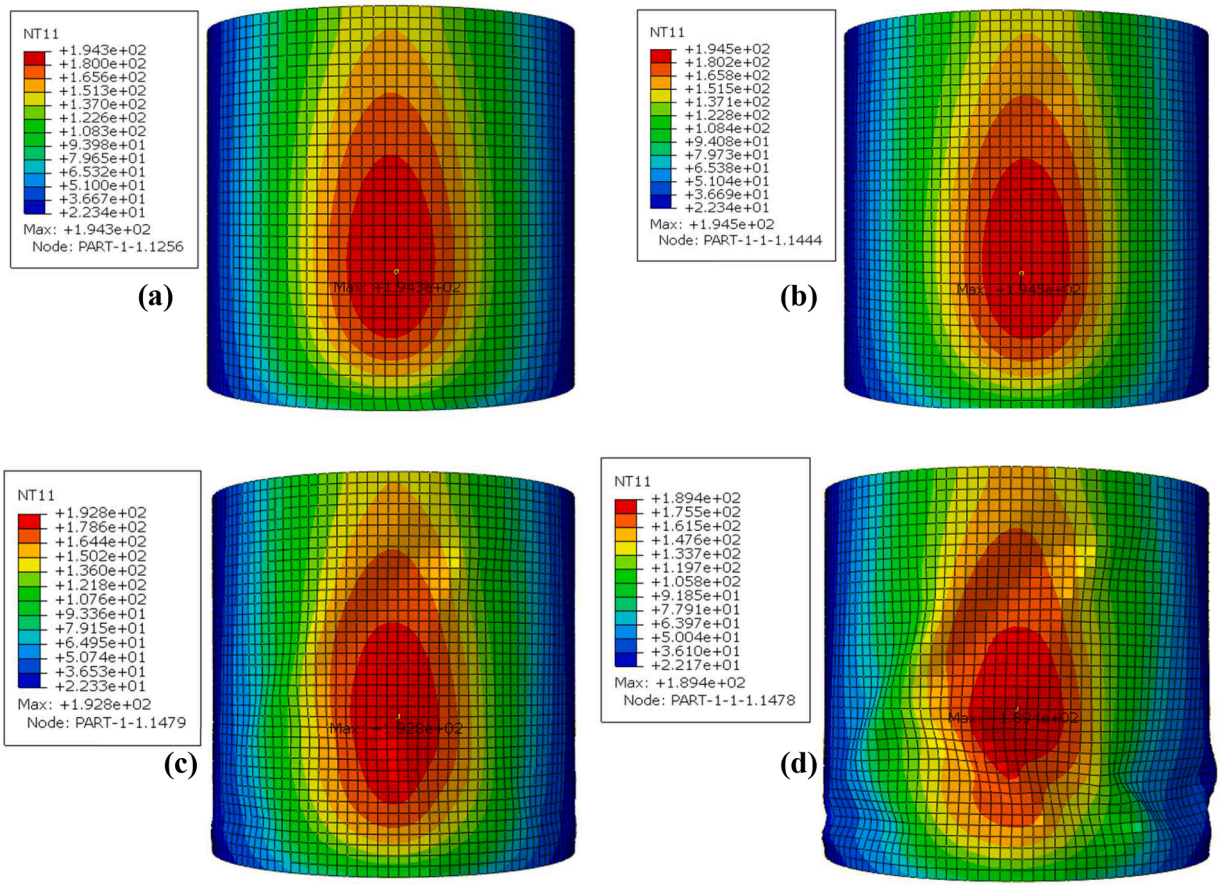

Fig. 20. Finite element analysis results of Stage II, (a) DS_1; (b) DS_2; (c) DS_3; (d) DS_4.

Table 9
Comparative analysis results of Stage-II (DS_1).

	Thermocouple 4 (°C)	Thermocouple 5 (°C)	Thermocouple 6 (°C)
Experiment	145.281	180.276	145.334
FEA	148.962	191.805	151.725
Error	+2.534 %	+6.395 %	+4.397 %

Table 10
Comparative analysis results of Stage-II (DS_2).

	Thermocouple 4 (°C)	Thermocouple 5 (°C)	Thermocouple 6 (°C)
Experiment	142.581	175.681	141.352
FEA	149.167	189.513	150.318
Error	+4.619 %	+7.873 %	+6.343 %

Table 11
Comparative analysis results of Stage-II (DS_3).

	Thermocouple 4 (°C)	Thermocouple 5 (°C)	Thermocouple 6 (°C)
Experiment	139.388	177.276	140.552
FEA	149.689	191.371	148.287
Error	+7.3901 %	+7.951 %	+5.503 %

Table 12
Comparative analysis results of Stage-II (DS_4).

	Thermocouple 4 (°C)	Thermocouple 5 (°C)	Thermocouple 6 (°C)
Experiment	139.241	173.276	141.334
FEA	151.748	188.016	146.468
Error	+8.982 %	+8.506 %	+3.632 %

respectively. Compared with intact tanks, the temperature distribution of pre-damaged tanks is more uneven.

To validate the reliability of the FEA model, a comparison was developed between the data collected by thermocouples 4, 5, and 6 and the simulation results, which are stated in Tables 9-12. Comparative analysis results show that the simulation results are in good agreement with the experimental results, and the error is within 2.5 %~8.9 %.

5.4.2. *Coupling failure analysis*

For fire scenario 1, the maximum tank shell temperature may not have reached the critical temperature of the SCT. Therefore, to ensure the effectiveness of the coupled failure analysis, the flame temperature is set at 920 ℃, and the corresponding analysis results are shown in Fig. 21 and Table 13.

As shown in Fig. 21(a), the temperature curves of different seismic damage states are similar, of which the maximum tank shell temperatures of DS_1, DS_2, DS_3, DS_4 tanks are 340.886 °C, 337.706 °C, 336.854 °C, 324.259 °C, respectively. The radial displacement abrupt change point [46,47,52] is adopted to assess the failure of SCTs under the coupling effects of earthquake and fire. As shown in Fig. 21(b,c), there are significant differences in the fire resistance times and critical temperatures among different seismic damage states. The fire resistance times of DS_1, DS_2, DS_3, DS_4 tanks are 56.047 s, 48.676 s, 39.882 s and 28.641 s, respectively. The critical temperatures of DS_1, DS_2, DS_3, DS_4 tanks are 287.171 °C, 261.342 °C, 223.631 °C and 192.912 °C, respectively. It can be observed that the prior-acting seismic damage can affect

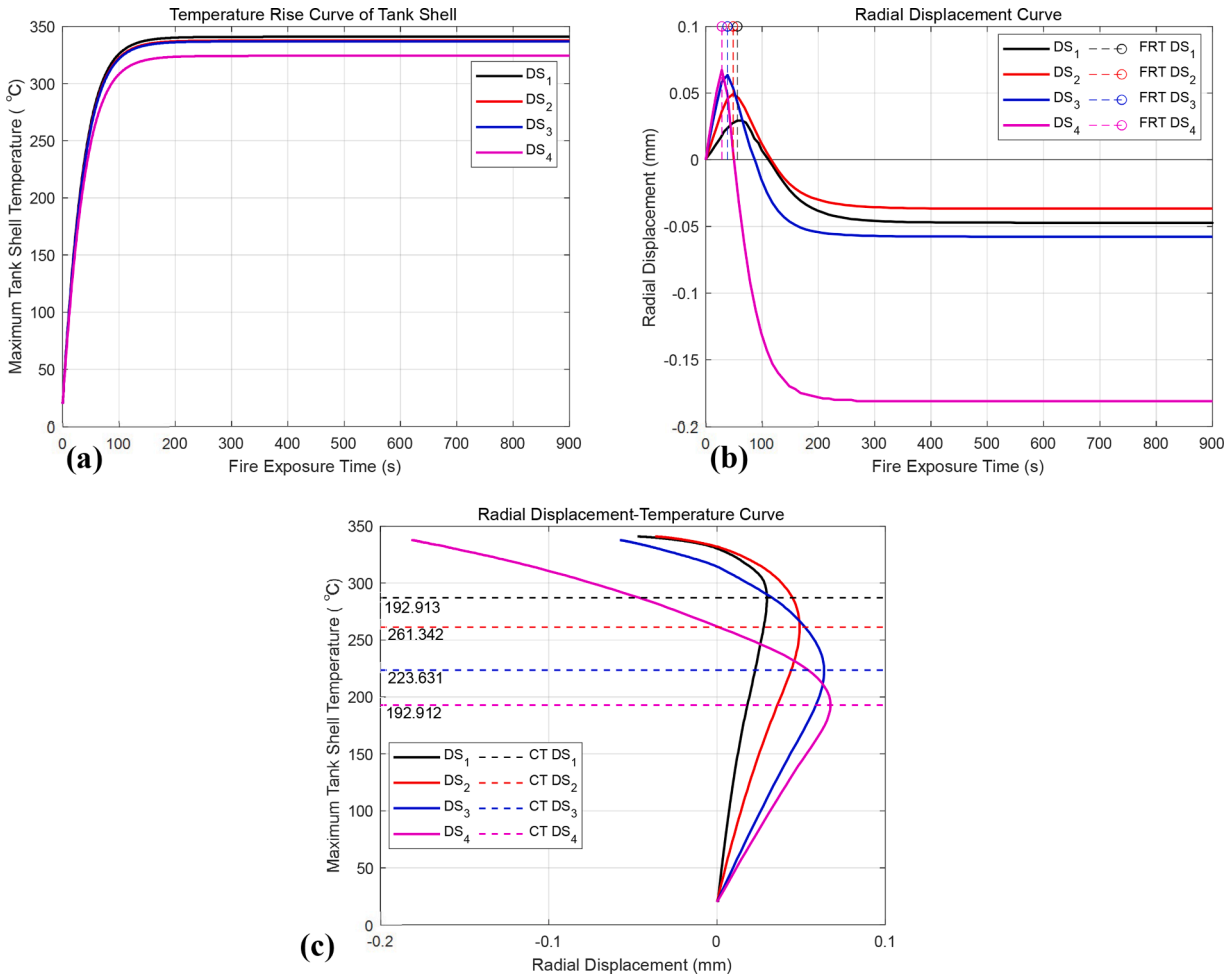

Fig. 21. Coupling failure analysis results, (a) Temperature rise curve of tank shell; (b) Radial displacement curve (FRT: Fire-resistant Time); (c) Radial displacement-temperature curve (CT: Critical Failure Temperature).

Table 13
Quantification of fire resistance attenuation.

Damage State	DS_1	DS_2	DS_3	DS_4
Fire Resistance Time (s)	56.047	48.676	39.882	28.641
Critical Temperature (°C)	287.171	261.342	223.631	192.912
Attenuation coefficients α	1	0.868	0.716	0.511
Attenuation coefficients β	1	0.910	0.779	0.672

the fire resistance of SCTs. In addition, as the severity of seismic damage to the tank increases, the fire resistance attenuation becomes more significant. The seismic pre-damage results in the generation of residual stress inside the storage tank. These residual stresses can affect the load-carrying capacity and deformation behavior of the tank under fire conditions. To be specific, for damage state DS_1, DS_2, DS_3, DS_4, the following fire resistance time attenuation coefficients α and critical temperature attenuation coefficients β can be obtained.

6. Conclusions

In this work, a two-stage experimental program and the corresponding finite element analysis (FEA) model were executed to expound the failure mechanism of steel cylindrical tanks (SCTs) exposed to the earthquake-fire sequence. The reliability of the FEA model was validated through comparative analysis, with errors spanning from 2.0 % to 13.4 %. Experiments and numerical results indicate that the seismic damage leads to a significant fire resistance attenuation of SCTs. The main causes of fire resistance attenuation were analyzed from the aspects of geometric deformation, residual stress, thermal radiation absorption capacity, etc. Based on the radial displacement abrupt failure criterion, the fire resistance time attenuation coefficients (0.868, 0.716, 0.511) and the critical temperature attenuation coefficients (0.910, 0.779, 0.672) were calculated to quantify the fire resistance attenuation caused by minor, moderate and severe seismic damage, respectively. As the severity of seismic damage to the tank increases, the fire resistance attenuation becomes more significant.

Through this experimental and numerical study, the mutually amplified phenomena associated with earthquake-triggered fire domino scenarios were revealed from the perspective of hazard-affected objects. The coupling effects between an earthquake and fire can significantly aggravate the escalation of domino accidents, leading to a non-linear risk superposition process. The prevention and mitigation of the E-FDSs require the full consideration of multiple factors such as the intensity of earthquakes and fires, equipment parameters, environmental characteristics, etc. This work provides fundamental prior knowledge to further develop the equipment fragility analysis and regional risk analysis under the earthquake-fire coupling effects, which is pivotal for preventing and mitigating the E-FDSs.

CRediT authorship contribution statement

Jinkun Men: Writing – review & editing, Writing – original draft, Validation, Methodology, Investigation, Conceptualization. **Guohua Chen:** Funding acquisition, Supervision, Writing – review & editing.

Genserik Reniers: Writing – review & editing. **Yue Wu:** Investigation. **Hailing Huang:** Investigation.

Declaration of competing interest

The authors declare that they have no known competing financial interests or personal relationships that could have appeared to influence the work reported in this paper.

Data availability

Data will be made available on request.

Acknowledgments

This study was supported by the National Natural Science Foundation of China (22078109), the Key-Area Research and Development Program of Guangdong Province (2019B111102001), the China Scholarship Council (202206150061).

References

[1] Men J, Chen G, Zeng T. Multi-hazard coupling effects in chemical process industry—part I: preliminaries and mechanism. IEEE Syst J 2023;17:1626–36.
[2] Men J, Chen G, Yang Y, Genserik R. An event-driven probabilistic methodology for modeling the spatial-temporal evolution of natural hazard-induced domino chain in chemical industrial parks. Reliab Eng Syst Saf 2022;226:108723.
[3] Men J, Chen G, Reniers G, Rao X, Zeng T. A hybrid deep belief network-based label distribution learning system for seismic damage estimation of liquid storage tanks. Process Saf Environ Protect 2023;172:908–22.
[4] Misuri A, Cozzani V. A paradigm shift in the assessment of Natech scenarios in chemical and process facilities. Process Saf Environ Protect 2021;152:338–51.
[5] Misuri A, Ricci F, Sorichetti R, Cozzani V. The effect of safety barrier degradation on the severity of primary Natech scenarios. Reliab Eng Syst Saf 2023;235:109272.
[6] Girgin S. The natech events during the 17 August 1999 Kocaeli earthquake: aftermath and lessons learned. Nat Hazards Earth Syst Sci 2011;11:1129–40.
[7] Ricci F, Moreno VC, Cozzani V. A comprehensive analysis of the occurrence of Natech events in the process industry. Process Saf Environ Protect 2021;147:703–13.
[8] Nishino T, Imazu Y. A computational model for large-scale oil spill fires on water in tsunamis: simulation of oil spill fires at Kesennuma Bay in the 2011 Great East Japan Earthquake and Tsunami. J Loss Prev Process Ind 2018;54:37–48.
[9] Chen G, Huang K, Zou M, Yang Y, Dong H. A methodology for quantitative vulnerability assessment of coupled multi-hazard in chemical industrial park. J Loss Prev Process Ind 2019;58:30–41.
[10] Lan M, Gardoni P, Qin R, Zhang X, Zhu J, Lo S. Modeling NaTech-related domino effects in process clusters: a network-based approach. Reliab Eng Syst Saf 2022;221:108329.
[11] Men J, Chen G, Zeng T. Multi-hazard coupling effects in chemical process industry—part II: research advances and future perspectives on methodologies. IEEE Syst J 2023;17:1637–47.
[12] Wang J, He Z, Weng W. A review of the research into the relations between hazards in multi-hazard risk analysis. Nat Hazards 2020;104:2003–26.
[13] Shi P. Regional disaster system (editor). In: Shi P, editor. Disaster risk science. Singapore: Springer Singapore; 2019. p. 49–96.
[14] Talebi E, Korzen M, Hothan S. The performance of concrete filled steel tube columns under post-earthquake fires. J Constr Steel Res 2018;150:115–28.
[15] Vitorino H, Rodrigues H, Couto C. Evaluation of post-earthquake fire capacity of reinforced concrete elements. Soil Dyn Earthq Eng 2020;128:105900.
[16] Alasiri MR, Chicchi R, Varma AH. Post-earthquake fire behavior and performance-based fire design of steel moment frame buildings. J Constr Steel Res 2021;177:106442.
[17] Shah AH, Sharma UK, Bhargava P. Outcomes of a major research on full scale testing of RC frames in post earthquake fire. Constr Build Mater 2017;155:1224–41.
[18] Wang Y-H, Tang Q, Su M-N, Tan J-K, Wang W-Y, Lan Y-S, Luo W, Zhou Y. Post-earthquake fire performance of square concrete-filled steel tube columns. Thin-Walled Struct 2020;154:106873.
[19] Calayir M, Selamet S, Wang YC. Post-earthquake fire performance of fire door sets. Fire Saf J 2022;130:103589.
[20] Lou T, Wang W. Mechanical properties of mild steel under combined effects of pre-damage and elevated temperatures in post-earthquake fire scenarios. J Constr Steel Res 2022;189:107102.
[21] Kourniotis SP, Kiranoudis CT, Markatos NC. Statistical analysis of domino chemical accidents. J Hazard Mater 2000;71:239–52.
[22] Darbra RM, Palacios A, Casal J. Domino effect in chemical accidents: main features and accident sequences. J Hazard Mater 2010;183:565–73.
[23] Abdolhamidzadeh B, Abbasi T, Rashtchian D, Abbasi SA. Domino effect in process-industry accidents – an inventory of past events and identification of some patterns. J Loss Prev Process Ind 2011;24:575–93.
[24] Huang K, Chen G, Yang Y, Chen P. An innovative quantitative analysis methodology for Natech events triggered by earthquakes in chemical tank farms. Saf Sci 2020;128:104744.
[25] Chen C, Reniers G, Khakzad N. A dynamic multi-agent approach for modeling the evolution of multi-hazard accident scenarios in chemical plants. Reliab Eng Syst Saf 2021;207:107349.
[26] Cozzani V, Reniers G. 1 - historical background and state of the art on domino effect assessment. In: Reniers G, Cozzani V, editors. Domino effects in the process industries. Amsterdam: Elsevier; 2013. p. 1–10.
[27] Cozzani V, Gubinelli G, Antonioni G, Spadoni G, Zanelli S. The assessment of risk caused by domino effect in quantitative area risk analysis. J Hazard Mater 2005;127:14–30.
[28] Zeng T, Chen G, Reniers G, Men J. Developing a barrier management framework for dealing with Natech domino effects and increasing chemical cluster resilience. Process Saf Environ Protect 2022.
[29] Men J, Jiang P, Zheng S, Kong Y, Zhao Y, Sheng G, Su N, Zheng S. A multi-objective emergency rescue facilities location model for catastrophic interlocking chemical accidents in chemical parks. IEEE Trans Intell Transp Syst 2020;21:4749–61.
[30] Men J, Chen G, Chen P, Zhou L. A Gaussian type-2 fuzzy programming approach for multicrowd congestion-relieved evacuation planning. IEEE Trans Intell Transp Syst 2022;23:20978–90.
[31] Spritzer JM, Guzey S. Review of API 650 Annex E: design of large steel welded aboveground storage tanks excited by seismic loads. Thin-Walled Struct 2017;112:41–65.
[32] Hernandez-Hernandez D, Larkin T, Chouw N. Shake table investigation of nonlinear soil–structure–fluid interaction of a thin-walled storage tank under earthquake load. Thin-Walled Struct 2021;167:108143.
[33] Krausmann E, Cruz AM. Impact of the 11 March 2011, Great East Japan earthquake and tsunami on the chemical industry. Nat Hazards 2013;67:811–28.
[34] Miladi S, Razzaghi MS. Failure analysis of an un-anchored steel oil tank damaged during the Silakhor earthquake of 2006 in Iran. Eng Fail Anal 2019;96:31–43.
[35] Ozdemir Z, Souli M, Fahjan YM. Application of nonlinear fluid–structure interaction methods to seismic analysis of anchored and unanchored tanks. Eng Struct 2010;32:409–23.
[36] Razzaghi MS. Chapter three - seismic performance of liquid storage tanks (editor). In: Fingas M, editor. Above ground storage tank oil spills. Gulf Professional Publishing; 2023. p. 89–131.
[37] Yoshida S. Earthquake damages and disaster prevention of aboveground storage tanks. EPI Int J Eng 2018;1:87–93.
[38] Malhotra PK, Wenk T, Wieland M. Simple procedure for seismic analysis of liquid-storage tanks. Struct Eng Int 2000;10:197–201.
[39] O'Rourke MJ, So P. Seismic fragility curves for on-grade steel tanks. Earthq Spectra 2000;16:801–15.
[40] D'Amico M, Buratti N. Observational Seismic Fragility Curves for Steel Cylindrical Tanks. J Press Vessel Technol 2018;141.
[41] Bezir F, Öztürk S, Sarı A, Akgül K. Fragility analysis of atmospheric storage tanks by observational and analytical data. Int J Steel Struct 2022:192–205.
[42] P. Ministry of Housing and Urban-Rural Development. Code for design of vertical cylindrical welded steel oil tanks (GB 50341-2014). Beijing: China Planning Press; 2014.
[43] Li X, Chen G, Khan F, Lai E, Amyotte P. Analysis of structural response of storage tanks subject to synergistic blast and fire loads. J Loss Prev Process Ind 2022;80:104891.
[44] Lai E, Zhao J, Li X, Hu K, Chen G. Dynamic responses and damage of storage tanks under the coupling effect of blast wave and fragment impact. J Loss Prev Process Ind 2021;73:104617.
[45] Cozzani V, Gubinelli G, Salzano E. Escalation thresholds in the assessment of domino accidental events. J Hazard Mater 2006;129:1–21.
[46] Li Y, Jiang J, Zhang Q, Yu Y, Wang Z, Liu H, Shu C-M. Static and dynamic flame model effects on thermal buckling: fixed-roof tanks adjacent to an ethanol pool-fire. Process Saf Environ Protect 2019;127:23–35.
[47] Li Y, Jiang J, Yu Y, Wang Z, Xing Z, Zhang Q. Thermal buckling of oil-filled fixed-roof tanks subjected to heat radiation by a burning tank. Eng Fail Anal 2022;138:106393.
[48] Shi G, Wang S, Chen X, Rong C. Post-fire mechanical properties of base metal and welds of Q235 steel. J Constr Steel Res 2021;183:106767.
[49] Li X, Chen G, Amyotte P, Khan F, Alauddin M. Vulnerability assessment of storage tanks exposed to simultaneous fire and explosion hazards. Reliab Eng Syst Saf 2023;230:108960.
[50] Guo Z, Shu K, Gao B, Wei Z. J-C model based failure criterion and verification of Q235 steel. Explos Shock Waves 2018;38:1325–32.
[51] Guo Z, Shu K, Gao B, Wei Z. Dynamic constitutive relation based on J-C model of Q235 steel. Explos Shock Waves 2018;38:804–10.
[52] Lei Z, Guoqing C, Zhiyou S, Lei F, Shouxiang L. On the damage study of the thermal radiation of the large oil-tank fire accidents. J Saf Environ 2008;8:110–4.
[53] Santos FdS, Landesmann A. Thermal performance-based analysis of minimum safe distances between fuel storage tanks exposed to fire. Fire Saf J 2014;69:57–68.